Experimental Evaluation of an Axillary Microwave Imaging System to Aid Breast Cancer Staging

Daniela M. Godinho, João M. Felício, *Member, IEEE*, Carlos A. Fernandes, *Senior Member, IEEE*, and Raquel C. Conceição

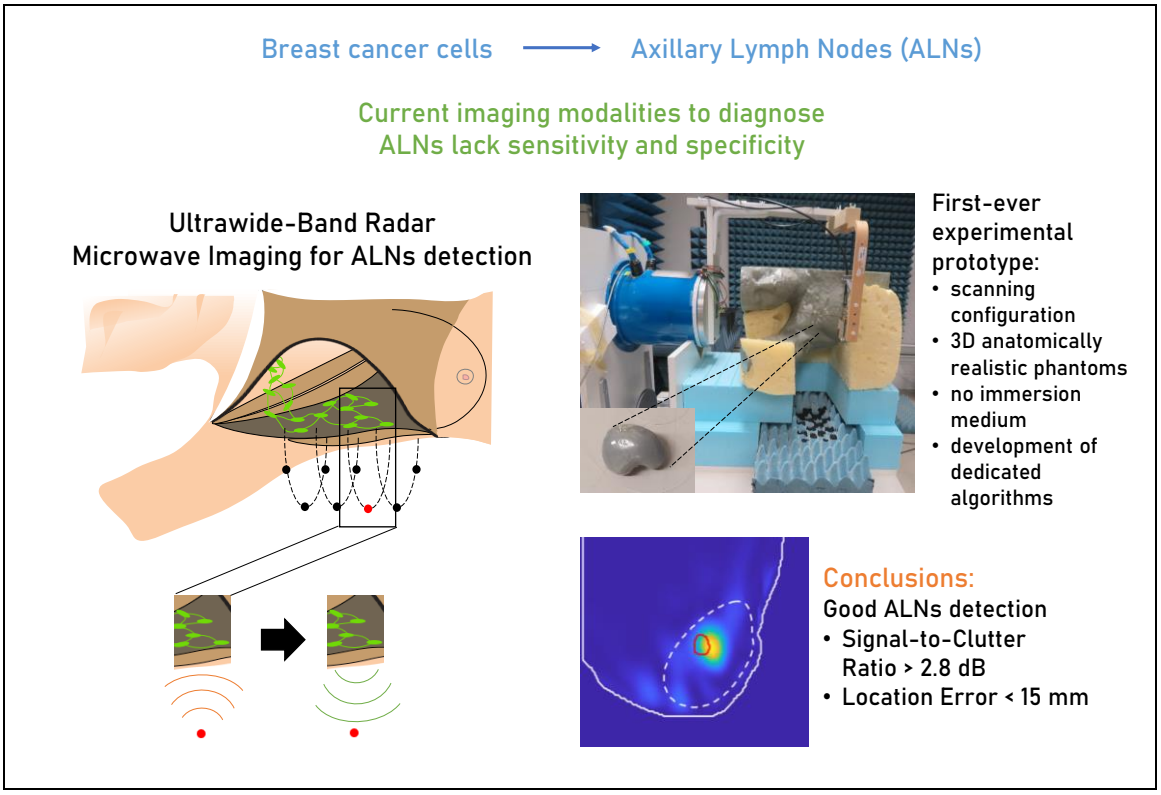

Novel Microwave Imaging System to Detect Axillary Lymph Nodes Metastasised by Breast Cancer.

Take-Home Messages

- This paper presents a new microwave imaging prototype which can be used as a complementary screening modality to aid breast cancer staging through the detection of axillary lymph nodes, addressing the main challenges of imaging an irregular body region with microwave technologies.
- The study confirms the potential of microwave imaging for the detection of axillary lymph nodes, showing imaging results with Signal-to-Clutter higher than 2.8 dB and a Location Error lower than 15 mm.
- The prototype and the methodology presented in this work is tailored for the axillary region application and can be a starting point for other irregular body regions microwave imaging applications.
- The present work is a significant contribution to the development of a microwave imaging system suited to image the axillary region, from the phantom development, antenna-positioning configuration to the dedicated imaging algorithm design.

Experimental Evaluation of an Axillary Microwave Imaging System to Aid Breast Cancer Staging

Daniela M. Godinho, João M. Felício, *Member, IEEE*, Carlos A. Fernandes, *Senior Member, IEEE*, and Raquel C. Conceição

***Abstract*—The number of metastasised Axillary Lymph Nodes (ALNs) is a key indicator for breast cancer staging. Its correct assessment affects subsequent therapeutic decisions. Common ALN screening modalities lack high enough sensitivity and specificity. Level I ALNs produce detectable backscattering of microwaves, opening the way for Microwave Imaging (MWI) as a complementary screening modality. Radar-based MWI is a low-cost, non-invasive technique, widely studied for breast cancer and brain stroke detection. However, new specific challenges arise for ALN detection, which deter a simple extension of existing MWI methods. The geometry of the axillary region is more complex, limiting the antenna travel range required for maximum resolution. Additionally, unlike breast MWI setups, it is impractical to use liquid immersion to enhance energy coupling to the body; therefore, higher skin reflection masks ALNs response. We present a complete study that proposes dedicated imaging algorithms to detect ALNs dealing with the above constraints, and evaluate their effectiveness experimentally. We describe the developed setup based on a 3D-printed anthropomorphic phantom, and the antenna-positioning configuration. To the authors' knowledge, this is the first ALN-MWI study involving a fully functional anatomically compliant setup. A Vivaldi antenna, operating in a monostatic radar mode at 2-5 GHz, scans the axillary region. Pre-clinical assessment in different representative scenarios shows Signal-to-Clutter Ratio higher than 2.8 dB and Location Error lower than 15 mm, which is smaller than considered ALN dimensions. Our study shows promising level I ALN detection results despite the new challenges, confirming MWI potential to aid breast cancer staging.**

***Keywords*—Axillary lymph nodes, axillary phantom, breast cancer, microwave imaging, pre-clinical assessment.**

I. Introduction

BREAST cancer is the most common cancer worldwide, accounting for approximately 2.26 million new cases in 2020 [1]. In most breast cancer cases in stages II to IV, the tumour can drain cancer cells to surrounding lymph nodes, specifically via Axillary Lymph Nodes (ALNs). The number of metastasised ALNs is considered in breast cancer staging and is important in subsequent therapeutic decisions [2].

Pre-surgical and non-invasive medical imaging techniques such as Ultrasound [3] and Magnetic Resonance Imaging [4], [5] are often used to assess axillary staging as part of the screening process. The used methods vary among countries, their own protocols, and available equipment, but generally lack high enough sensitivity and specificity. The more accurate procedure is Sentinel Lymph Node Biopsy (SLNB), where surgeons remove the sentinel node, the first lymph node receiving drainage from the tumour. Studies show that in around 70% [6], [7] of the procedures, SLNB yields a negative result when it could have been avoided. If the pathological analysis result of SLNB is positive for metastases, or in case of prior positive medical imaging results and ultrasound-guided biopsy confirmation, Axillary Lymph Node Dissection (ALND) may be performed. ALND consists of partial or complete removal of ALNs, which can lead to patients' slower recovery, increased risk of infection, lymphedema, and/or paraesthesia [8], [9]. False positive imaging results without biopsy would lead to pre-emptive lymph node removal and, therefore, unnecessary patients' morbidity. This justifies the need for the development of effective auxiliary ALNs screening techniques, preferably non-invasive.

We evaluate the feasibility of Microwave Imaging (MWI) to become an alternative imaging technique for the detection of level I ALNs - the ALNs more likely to receive drainage from tumour cells first - owing to its potential to reduce the false negative results of current imaging modalities. MWI is based on dielectric properties contrast existing between different tissues composing the body. MWI has been studied for other medical applications, including early breast cancer and brain stroke detection, showing promising results [10]–[14]. MWI has advantages when compared to other imaging modalities, namely for using non-ionising radiation, being non-invasive, with good sensitivity and specificity, relatively low-cost, and potentially user-independent.

However, ALN-MWI presents several challenges when compared to breast and brain MWI: 1) the torso limits the antenna scan range required for acceptable image resolution; 2) it is no longer practical to use liquid immersion to minimise skin reflections that hide ALN response, unlike most breast MWI setups [10]–[12]; moreover, we require a contactless system to minimise sanitation issues; 3) the shape of the axillary region has both concave and convex surfaces that tend to undermine the effectiveness of traditional skin reflection (artefact) removal algorithms; 4) level I ALNs may be close to the skin, making it more difficult for artefact removal

Manuscript submitted January 15, 2021; revised April 21, 2021, accepted July 1, 2021. This work is supported by Fundação para a Ciência e a Tecnologia - FCT under fellowship SFRH/BD/129230/2017, FCT/MEC (PIDDAC) under the Strategic Programme UIDB/00645/2020, and also in part by FEDER-PT2020 Partnership Agreement under Grant UIDB/EEA/50008/2020.

Daniela M. Godinho and Raquel C. Conceição are with Instituto de Biofísica e Engenharia Biomédica, Faculdade de Ciências da Universidade de Lisboa, 1749-016 Lisbon, Portugal (e-mail: dgodinho94@gmail.com, raquelcruzconceicao@gmail.com).

João M. Felício is with Centro de Investigação Naval (CINAV), Escola Naval, Almada, Portugal, and with Instituto de Telecomunicações, Instituto Superior Técnico, Universidade de Lisboa, Lisbon, Portugal (e-mail: joao.felicio@lx.it.pt).

Carlos A. Fernandes is with Instituto de Telecomunicações, Instituto Superior Técnico, Universidade de Lisboa, Lisbon, Portugal (e-mail: carlos.fernandes@lx.it.pt).

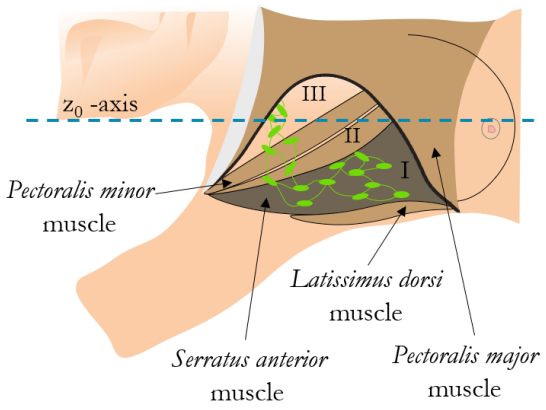

Fig. 1. Simplified representation of lymph nodes levels, and surrounding muscles. The positioning of the patient is the same as that used during the examination, with the patient lying on one side, with the arm along the head.

algorithms to discriminate between skin and ALNs; 5) level I ALNs are usually in the vicinity of muscles that may have comparable MW response.

Fig. 1 shows ALNs hierarchical levels, and their positions relative to the surrounding muscles. ALNs can be classified in three levels based on their relative anatomical location. Level I ALNs are usually located in fatty tissue, and lateral to the lateral border of the *pectoralis minor* muscle. Level I ALNs are usually the first nodes affected by breast cancer metastasis, in circa 97% of the cases [15], [16]. Their depth, i.e. their distance to skin, ranges from 14 to 80 mm [17] depending on each patient's Body Mass Index (BMI), although no detailed relationship has been reported yet [18], [19]. Level II nodes are located between lateral and medial margins of the *pectoralis minor* muscle, and level III nodes are medial to the medial margin of the *pectoralis minor* muscle and inferior to the clavicle [2]. Due to excessive biological tissue attenuation and low contrast against muscles, deeper, higher than hierarchical level I ALNs cannot be screened using MWI.

A healthy ALN has a kidney-like shape and its size can range from 1 to 25 mm in its largest axis [20]. Typical signs of metastases in ALNs are the absence of a fatty region called the hilum, the increase of the cortex thickness, and its tendency to resemble a spherical shape with non-defined margins [21], [22]. Until now, information about dielectric properties of ALNs is very limited. Some authors have addressed this topic in the last decades [23]–[25] but their studies either have reduced number of samples, contain possible contamination by surrounding fat tissue, or lack detail about the measurement accuracy and confounders' influence.

Eleutério *et al.* [26] presented a feasibility study of ALN-MWI with results showing good detection of isolated ALNs and good distinction between modelled healthy and metastasised ALNs. However, the study was based on simulations in a 2D-geometry only, where antennas laid in contact with a planar boundary representing the skin. It did not consider the effect of non-uniform 3D-shape of the axillary region, nor the influence of the measurement setup.

In this paper, we present a pre-clinical system for the detection of level I ALNs. The proposed ALN-MWI system comprises a single antenna with its position scanning system, the RF equipment, the control and signal acquisition components, and signal post-processing algorithms developed to address the challenges listed earlier in this section. The antenna operates in air without coupling medium, and without body contact, similarly to dry imaging setups for breast MWI that have been proposed [27]–[30]. The ALN-MWI system is tested with an anthropomorphic phantom of the axillary region and torso with embedded level I ALN models. The configuration approaches as much as possible an actual clinical scenario, where the patient undergoes the MWI exam of the axillary region lying sideways on one of the arms, which is extended along the head. For validation purposes, we present and discuss the results obtained using this system for three locations of level I ALNs in the phantom, using common metrics. No muscles are considered in this stage of the study. To the best of our knowledge, this is the first comprehensive study ever presented in this topic, and the first realistic ALN-MWI experimental system.

In the remainder of this paper, we describe the experimental setup, the anatomically realistic phantoms and materials in Section II. We present the algorithms implemented for data processing in Section III, the results are presented and discussed in Section IV, and the main conclusions are drawn in Section V.

II. Experimental Setup and Materials

This section presents the details of the proposed MWI system and the anthropomorphic phantoms.

A. Phantom development

Our anatomically realistic phantom of the axillary region was 3D-printed from a processed image of a patient's Computed Tomography (CT). The BMI of the patient was 19 kg/m^2, which is considered as normal weight. Only a region of the image was selected to be printed, comprising the head (for reference purposes), a part of the arm, and the torso from the neck to under the breast (Fig. 2). The phantom was hollow, and was printed in parts using an Ultimaker 3 Extended 3D-printer. The printing material was PolyLactic Acid (PLA), which has permittivity values ranging from 2.75 to 2.9 and a loss tangent of 0.01 [31]. The parts were glued and impermeabilised using epoxy resin. The axillary part was a container that held the tissue mimicking liquid. The phantom had an opening in the yz-plane to enable easy access to the container (Fig. 2(b)). No skin layer was added to the phantom wall. The air/phantom artefact is similar to the response of an actual skin layer, but with a few dB lower magnitude [27]. Other authors have also used phantoms without skin to validate their systems [14], [32].

The ALN model was created using an open-source STL model of a kidney [33]. The model was reshaped and resized to fit metastasised ALNs characteristics. Its dimensions were set as $23.6 \times 17.6 \times 12$ mm, as shown in Fig. 3(a). It was 3D-printed with a 1.2 mm thickness wall and filled with a tissue mimicking mixture through a 1 mm aperture that was subsequently sealed with epoxy resin. The ALN was placed

(a) (b)

Fig. 2. 3D printed body phantom in (a) coronal view and (b) sagittal view. The blue shade represents the volume used for the image reconstruction that comprises the volume where level I ALNs were placed.

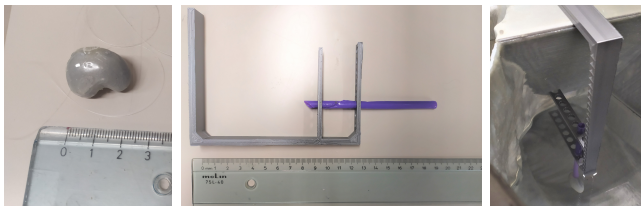

(a) (b) (c)

Fig. 3. 3D-printed (a) phantom of metastasised ALN, and (b) plastic support designed to control the ALN positioning. (c) shows an example of ALN positioning inside the phantom.

inside the phantom connected by a nylon string that was fixed in a known position with the help of a plastic support (Fig. 3(b-c)). The ALN was placed in three locations within the phantom and was also positioned at depths varying between 20 to 30 mm from the phantom surface, which corresponds approximately to the depth range of a level I ALN for a woman of normal weight.

B. Tissue mimicking materials

Although information about ALNs dielectric characteristics is still limited, existing results indicate that healthy ALNs have similar properties to breast fibroglandular tissue while metastasised ALNs have increased relative permittivity (ϵ_r) and conductivity (σ) [25], [34].

In this study, mixtures of TX-100, distilled water and sodium chloride (NaCl) were used in the proportions reported by Joachimowicz et al. [35] to create fat (G3) and ALN (T) tissue mimicking mixtures, respectively. Dielectric properties of $\epsilon_r = 4$ and 55 and $\sigma = 0.01$ and 3.5 S/m for fat [36], [37] and ALN, respectively, at 4 GHz, were verified using an open-ended coaxial probe.

C. Antenna and data acquisition

The setup used Ultra-Wide Band (UWB) low-power radar pulses in a monostatic configuration. An ENA Series Network Analyser, Agilent E5071C, was used for the RF measurements. The signals were measured with a testing power of 10 dBm and signal IF bandwidth of 7 kHz. A single Vivaldi antenna was used in the setup, impedance-matched in the $2-5$ GHz frequency band [38], calibrated with a Keysight Electronic

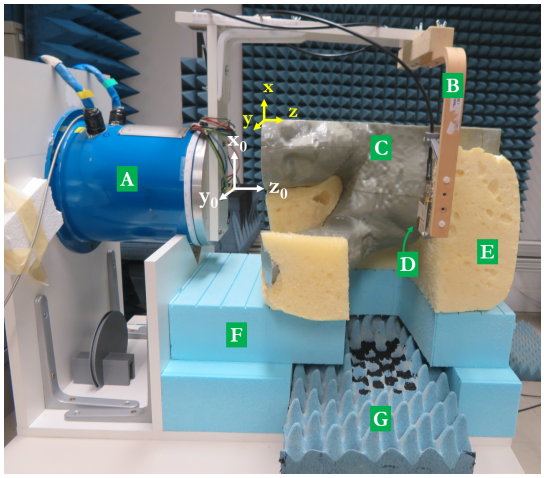

(a)

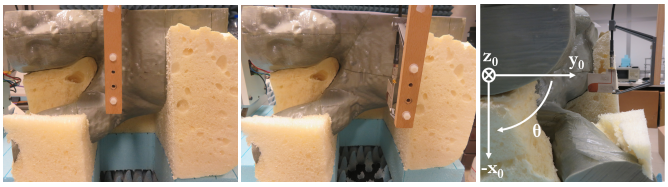

(b) (c) (d)

Fig. 4. Measurement setup (a) with all components (roll positioner [A], antenna support arm [B], phantom [C] and the antenna [D]). (b) shows the first horizontal and angular position of the antenna, (c) and (d) show its last horizontal and first angular position in the coronal and axial views, respectively. The yellow and blue pieces [E, F] supporting the phantom are styrofoam. The blue piece at the bottom [G] is an Eccosorb CV type microwave absorber, which is used for testing purposes to minimise the table's reflection. The white coordinate system in (a) and (d) is used for the rotation and translation movements of the arm and antenna, and the yellow coordinate system in (a) is used for the image reconstruction algorithm.

Calibration (E-cal). The antenna was attached to an angular positioner through an adjustable arm that enabled scanning a cylindrical area around the axillary region (Fig. 4). Due to the torso shape, the antenna can only scan a 90° angular range. The radial distance between each antenna position and the phantom surface ranged from 4 to 56 mm, with an average distance of 35 mm.

A total of 72 monostatic signals were recorded at 9 angular positions (10° step) and at 8 horizontal positions (10 mm step). This measurement grid is onwards referred to as $\mathbf{G}_{\mathrm{M}}$, as shown in Fig. 5(a). A free-space measurement was also performed for calibration purposes. A total of $N_f = 1401$ frequency points were acquired for each antenna position.

III. Signal and Image Processing Algorithms

In this section, we present the formulation of the algorithms used for artefact removal and image reconstruction, which were specifically adapted for the axillary imaging application. The volume of interest of the axillary region is smaller than the volume of the experimental phantom and this needs to be accounted for algorithm development. We also present the performance metrics we used to evaluate the system response and a methodology to optimise which subset of antenna positions shall be used for image reconstruction.

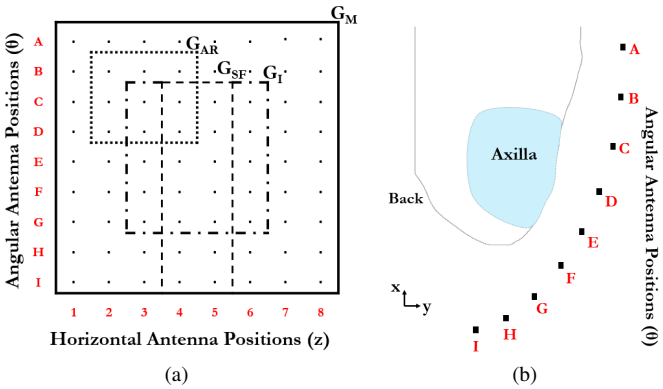

(a) (b)

Fig. 5. (a) Flattened view of cylindrical antenna position grid; (b) angular antenna positions on the axial plane of the axillary phantom. In (a) $\mathbf{G}_{\mathrm{M}}$ (delimited by solid line) designates the set of all points of the measurement grid; $\mathbf{G}_{\mathrm{AR}}$ (delimited by dotted line) is an example of the subset of neighbour antennas used for artefact removal for (C,3) antenna position; $\mathbf{G}_{\mathrm{SF}}$ (delimited by dashed line) is the subset used to create the spatial filter; and $\mathbf{G}_{\mathrm{I}}$ (delimited by dash-dot line) represents the subset of antenna positions used for image reconstruction.

A. Artefact Removal Algorithm

A single measurement in free-space was required to remove the antenna frequency response from the scattered signals [38]. Additionally, a detailed knowledge of the shape of the body is also of great importance for the algorithms. This can be retrieved using very low-cost optical devices such as a webcam [27] or more complex laser systems [39]. In our proposed methodology, this information was assumed available.

Backscattered signals contain high amplitude artefacts generated by air/dielectric interface at the phantom surface. These were removed using Singular Value Decomposition (SVD). SVD is a linear algebra method that computes the factorisation of a matrix. Given matrix $\mathbf{M}$ of dimensions $m \times n$, it can be decomposed as follows:

$$\mathbf{M} = \mathbf{U}\mathbf{\Sigma}\mathbf{V}^{*} \tag{1}$$

where $\mathbf{U}$ is a $m \times m$ unitary matrix, $\mathbf{\Sigma}$ is a $m \times n$ diagonal matrix with non-negative real non-increasing numbers σ_l, for $l = 1, \ldots, \min[m; n]$, and V is a $n \times n$ unitary matrix. The columns of $\mathbf{U}$ and $\mathbf{V}$ are called the left-singular and right-singular vectors of $\mathbf{M}$, respectively, and the values σ_l of $\mathbf{\Sigma}$ are called singular values of $\mathbf{M}$. The first q singular values represent the highest magnitude components contributing to the signal, which likely correspond to the air/phantom interface artefacts [27].

In the present problem, $\mathbf{M}$ was a $N_f \times N_a$ matrix where each column is the antenna-independent input reflection coefficient $\mathbf{s}_{a,h}$, obtained as the difference in linear units between the measured antenna input reflection coefficient in the presence of the body and the measurement in free-space [38]. N_f was the number of frequency points, a and h are the indices of each angular and horizontal antenna positions, respectively, and N_a was the number of antennas considered for the matrix factorisation.

The signals without the air/phantom response ($\mathbf{M}^{cal}$) can be obtained by subtracting the contribution from the first q singular values [27]:

$$\mathbf{M}^{cal} = \mathbf{M} - \sum_{l=0}^{q} \sigma_l \mathbf{u}_l \mathbf{v}_l^{*} \tag{2}$$

The resulting signals are designated $\mathbf{s}_{a,h}^{cal}$. The number of components q that need to be removed was found by an iterative process aiming to optimise the performance metrics of the produced images, in representative experimental tests. These tests comprised measurements with ALNs in known positions inside an axillary region phantom using the current antenna configuration. Once the value of q is determined, it can be applied for axillary regions with comparable shape where the target location is not known in advance.

Due to the wide range of distances from each antenna to the phantom surface, and owing to different surface slopes at the rays entry point in the phantom, matrix $\mathbf{M}$ actually contained only a subset $\mathbf{G}_{\mathrm{AR}}$ of antenna positions neighbouring the antenna under analysis. The factorisation of $\mathbf{s}_{a,h}$ was performed considering the surrounding 8 neighbours and the signal itself: $\mathbf{s}_{a+\Delta_N, h+\Delta_N}$, where $\Delta_N = -1, 0, 1$. This strategy improves the factorisation of the artefacts into separate singular vectors since each group of neighbour antennas shares similar shape of the phantom surface, and therefore corresponding responses are similar.

B. Image Reconstruction Algorithm

The imaging algorithm was based on wave migration, where the intensity of each voxel can be calculated as the following:

$$intensity(v) = \left[\sum_{a,h}^{N_a} \sum_{f}^{N_f} \mathbf{s}_{a,h}^{cal}(f) e^{2jk_0(d_{ahv}+d_e)} \right]^2 \tag{3}$$

where d_e is the electric length of the antenna, d_{ahv} is the electrical distance between each antenna position (a, h) and each voxel v, calculated as $d_{air,ahv} + \sqrt{\epsilon_{diel}} \times d_{diel,ahv}$, where $d_{air,ahv}$ is the corresponding distance travelled in air, $d_{diel,ahv}$ is the corresponding distance in the new phantom medium, and ϵ_{diel} is the corresponding refractive index. The wave number k_0 is calculated as $\frac{2\pi f}{c}$ for each frequency point f, with c as the speed of light.

Refraction effects were not considered in the image reconstruction algorithm, since their computation increased the computational cost and we verified in a separate study their effect on imaging results is not significant for this configuration [40]. For visualisation purposes, the results are represented in axial (xy), coronal (xz) and sagittal (yz) planes.

C. Spatial Filter

Only a sub-volume of the whole 3D region of the phantom filled with fat tissue-mimicking mixture is relevant. The region of interest should correspond roughly to the fat layer region where level I ALNs are located. The region of interest is shaded in blue in Fig. 2. A spatial filter (**SF**) was used to create this sub-volume analytically, regardless the antennas used for image reconstruction algorithm. As will be discussed ahead, the definition of the sub-volume is relevant to define performance metrics.

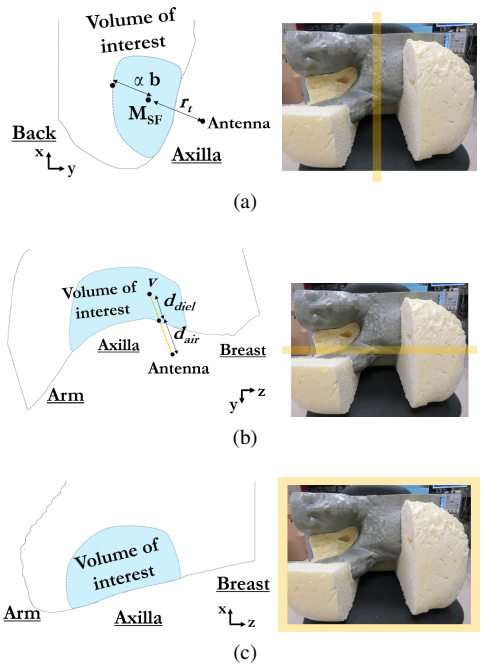

Fig. 6. Representation of the volume of interest for (a) axial, (b) sagittal, and (c) coronal planes. The blue shade represents the axillary region where lymph nodes have higher probability to be located. The yellow shade shows each represented plane in the phantom.

The **SF** filter was normalised so the maximum magnitude would be 1. The final image was obtained by multiplying the **SF** and the reconstructed image obtained from the wave migration algorithm. This assigns a higher weight to the voxels in the axillary region, which is the region of interest. The **SF** is a skewed Gaussian function resulting from the multiplication of a power function of exponent γ ($\mathbf{SF}_1$) and a piece-wise function with a Gaussian decay ($\mathbf{SF}_2$):

$$\mathbf{SF}_1 = \left(\frac{d_{diel,ahv}}{r_1}\right)^{\gamma} \tag{4}$$

$$\mathbf{SF}_2 = \begin{cases} 1, & \text{if } d_{\mathrm{SF},ahv} < r_t \\ \exp\left(-\left(\frac{d_{\mathrm{SF},ahv} - r_t}{r_2}\right)^2\right), & \text{otherwise} \end{cases} \tag{5}$$

where $d_{\mathrm{SF},ahv} = d_{air,ahv} + 2 \cdot d_{diel,ahv}$, which is neither a physical distance nor electrical distance, but instead a weighted distance in which a higher weight is given to $d_{diel,ahv}$, since the region of interest is close to the phantom surface. Parameters r_1, γ, r_t, and r_2 can be adjusted according to the region we aim to select and can be defined differently for each antenna position. Parameter r_1 is proportional to the magnitude of function $\mathbf{SF}_1$, γ determines the growth rate of function $\mathbf{SF}_1$, and r_t and r_2 define the threshold and the rate of the Gaussian decay of function $\mathbf{SF}_2$, respectively (Fig. 7).

In order to retrieve the phantom shape and create the corresponding volume of interest, the **SF** was created using a subset of the antenna positions ($\mathbf{G}_{\mathrm{SF}}$) comprising the horizontal antenna positions centred at the region of interest and the angular antenna positions closer to and surrounding the region of interest. The selected subset of antenna positions is chosen considering the volume of the axillary region under study.

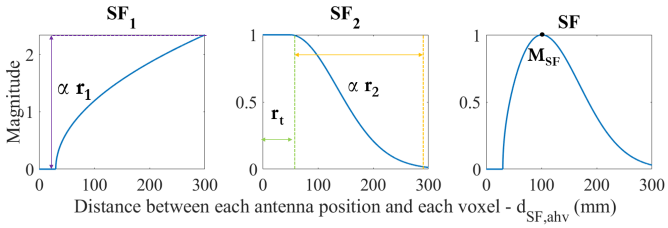

Fig. 7. Plot of each function of the spatial filter **SF** over the distance between an antenna position and a voxel ($d_{\mathrm{SF},ahv}$) for an arbitrary combination of parameters. M_{SF} represents the point of maximum magnitude.

D. Performance Evaluation

The performance of the current setup and algorithms was evaluated using metrics that quantify the quality of ALNs detection: Signal-to-Clutter Ratio (SCR), Signal-to-Mean Ratio (SMR), Full Width Half Maximum (FWHM) and Location Error (LE). The ALN response was identified with the maximum voxel value (M_{ALN}) of the volume of interest defined in the previous sections and its neighbouring voxels when they were above half of the maximum. SCR measures the contrast between M_{ALN} and the maximum value of clutter (clutter are local maxima originated by common and random reflections or unidentifiable sources). SMR is the ratio between M_{ALN} and the mean value of the clutter, measuring how easily the ALN can be identified within the image. FWHM measures the extent of the response by computing the average distance in 3D-space between the coordinates of M_{ALN} and the voxels where its response drops to half. LE is the distance between the coordinates of M_{ALN} and the centre of the true location of the ALN.

In line with other authors [11], [41], we require a SCR above 1.5 dB for positive detection. We consider LE acceptable if it is within the dimensions of the ALN.

E. Antenna Position Selection

The original grid of antenna positions ($\mathbf{G}_{\mathrm{M}}$) covers a larger volume in front of the phantom than the volume of interest. Depending on the location of the targets, some antenna positions may be far or with unfavourable signal paths to the target, penalising the reconstructed image quality. It is desirable to identify the best size of the subset of antenna positions for that reason. Because the location of the ALNs is not known *a priori* in a real application, an automated test can be run which successively tests different sizes of subsets $\mathbf{G}_{\mathrm{I}}$ of antenna positions, to maximise SCR and SMR.

As of now, the relationship between the number of antennas and the resulting imaging resolution was evaluated by visual inspection by maximising both SCR and SMR and minimising FWHM to acceptable dimensions, which gives a measure of the image resolution (e.g. a lower image resolution results in higher FWHM). A 5×4 grid of antenna positions (i.e. a total of 20 antennas) was found to provide the best results (a balance between the number of antennas, better resolution, less artefacts and optimised metrics), as represented in Fig. 5(a). This subset grid was then translated by one column or one line across the original antenna position grid ($\mathbf{G}_{\mathrm{M}}$) to

detect the ALNs in different locations. The resulting images are then analysed by visual inspection.

IV. Results and Discussion

This section presents the optimal parameters found for the imaging algorithms, which maximise the performance metrics of the reconstructed images. We present the resulting images and performance metrics of the experimental tests with one level I ALN embedded in fat mimicking material. We tested three different locations, named ALN-1, ALN-2 and ALN-3, represented in Fig. 8. ALN-1 is at a central position between the breast and the arm, ALN-2 is closer to the arm, and ALN-3 is closer to the breast. The distance between ALN-2 and ALN-3 is 48 mm. ALN-1 and ALN-3 are placed at an average depth from the phantom surface of ~ 30 mm, while ALN-2 is closer to the surface at ~ 20 mm depth.

A. Algorithms Parameters

The **SF** parameters were defined considering the anatomy of a patient with similar torso dimensions to our phantom. The subset of antenna positions ($\mathbf{G_{SF}}$) comprised the horizontal positions 4 to 5 (corresponding to 30% of the horizontal antenna positions) and the angular antenna positions C to I. We considered $r_1 = 75$ mm, $\gamma = 0.5$, $r_t = 0$ mm, and $r_2 = 120$ mm. Parameters r_t and r_1 were increased for angular antenna positions G to I since they are farther away from the region of interest than the others, assuming $r_1 = 400$ mm and $r_t = 50$ mm. This highlights a volume of interest extending from the phantom surface to a depth of approximately 40 mm in the phantom. The optimal subset of antenna positions $\mathbf{G}_{\mathrm{I}}$ to image the current axillary phantom was obtained with horizontal antenna positions 3 to 6 and angular antenna positions E to I (Fig. 5(a)). In a clinical scenario, the **SF** parameters, $\mathbf{G}_{\mathrm{SF}}$, and $\mathbf{G}_{\mathrm{I}}$ would need to be adjusted according to each patient's biometric information, such as the axillary region size and BMI. This would prevent the **SF** from influencing the results, namely by hiding ALNs.

Regarding the artefact removal, the number of components to be removed with SVD for each antenna position, which resulted in a reliable ALN detection for the three experimental tests, was determined as $q = 4$. Due to its non-uniform shape, the response of the phantom surface is present in more than one singular vector. The first singular vector contains the main reflection from the surface, with an average magnitude of 22. The remaining removed singular vectors present residual reflections with average magnitudes of 1.3, 0.9 and 0.7. The singular vectors that preserve the ALN response have average magnitudes below 0.5.

SVD yields good results for the performed tests for ALNs positioned at depths varying between 20 to 30 mm: in fact, results show that SVD is able to remove components with magnitudes up to 44 times higher than the ALN response, which is encouraging to trust the viability of a dry setup. The detection of shallower ALNs can be more challenging. In those cases, the ALN and the phantom surface response can be factorised in the same singular vector, hampering the ALN detection. Nonetheless, ALNs shallower than 20 mm are only observed in few cases of breast cancer patients [17].

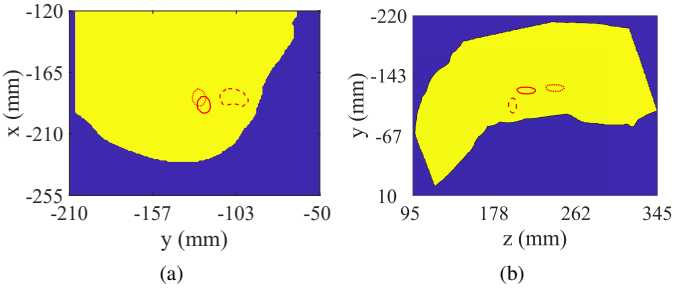

Fig. 8. Projection of phantom and lymph nodes positions on (a) axial, and (b) sagittal planes. Average contours of the phantom in yellow, ALN-1 in solid red line, ALN-2 in dashed red line and ALN-3 in dotted red line.

B. Imaging Results

Fig. 9(a-c) shows the reconstructed images on the main planes of ALN-1, using the **SF** presented before. We observe an adequate detection of the ALN with a SCR of 3.01 dB and LE of 11.40 mm, which is within the range of the ALN dimensions ($23.6 \times 17.6 \times 12$ mm). FWHM is larger than the average dimensions of the ALN. It is larger in the yz-plane due to the shape of the axillary region in that plane, which results in a lower cross-range resolution.

In order to better understand the impact of the **SF** on the imaging results, we show the corresponding reconstructed images when the **SF** is not applied in Fig. 9(d-f). Firstly, there is no significant impact on the peak intensity, as the gain of the filter is 1. Secondly, the arm and the breast regions present some additional clutter that is removed with the **SF**. The removal of such clutter is intentional, since ALNs are not expected in the arm or breast itself. Thirdly, the detected position of ALN-1 does not change with the SF, as it is detected at the same location as in Fig. 9(a-c). Finally, it is confirmed that the artefacts at the phantom surface are entirely removed with SVD and not with the help of the **SF**, which is only used to select the volume of interest.

It is also important to show the reconstructed images obtained when no ALN exists in the axillary phantom, with the **SF**, as in Fig. 9(g-i). We observe that the maximum magnitude of the reconstructed image with ALN (Fig. 9 (a-c)) is 39.6, whereas without ALN (Fig. 9 (g-i)) it is 17.7. This shows that MWI is sufficiently sensitive to the presence of an ALN, and, therefore, a promising technology for ALN screening. The images also allow observing the effect of the challenging shape of the axillary region. The concavity of this shape causes some artefacts in the region where ALNs are likely to be located. In fact, the more concave the shape is, the more challenging the artefact removal becomes. These artefacts are the major challenge for ALN-MWI, and one of the reasons why this study is relevant to the scientific community. In fact, in breast and head MWI, where the most advanced medical MWI systems are found, the shape of the body is much more regular, and artefacts and clutter are easier to overcome.

Both images of ALN-2 and ALN-3 produce similar performance as ALN-1. Images are not shown due to space constraints but a summary of the performance metrics is given in Table I. Both present a positive detection, having a SCR

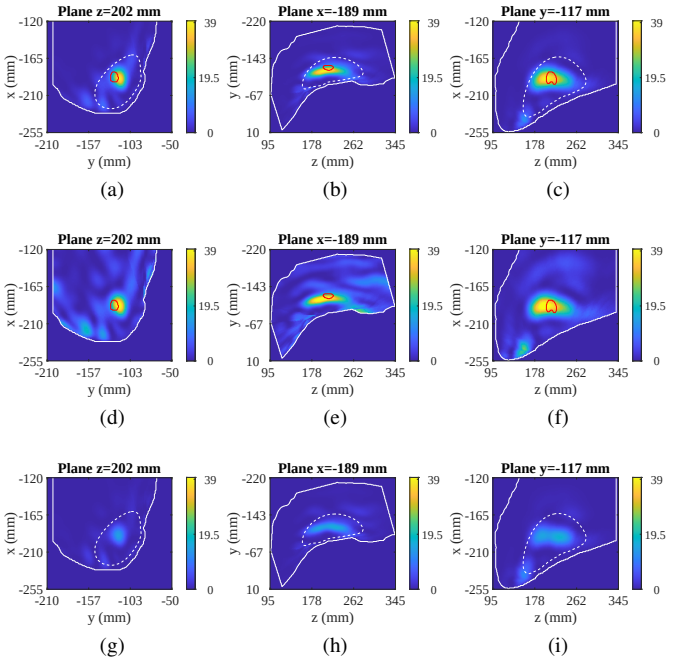

Fig. 9. Reconstructed images of the axillary region. The first and second row show the images of the axillary phantom with ALN-1 inside, when applying and not applying our proposed spatial filter, respectively, and the third row shows the images of the axillary phantom without ALNs and when applying the spatial filter. The first, second and third columns represent the axial, sagittal, and coronal planes, respectively. The approximate location and shape of the lymph node is represented as a red contour. The white solid and dashed contours correspond to the phantom limits and the volume of interest selected with the spatial filter, respectively.

TABLE I
PERFORMANCE METRICS OF THE PERFORMED TESTS.

	SCR (dB)	SMR (dB)	FWHM (mm)	LE (mm)
ALN-1	3.01	8.95	32.7	11.4
ALN-2	2.78	8.69	35.3	12.2
ALN-3	2.89	8.73	34.7	14.9

higher than 2.78 dB. LE and FWHM are slightly higher than the corresponding metrics for ALN-1. LE is still within the range of the ALN dimensions, although FWHM is slightly larger. This can be explained by their positioning in the axillary phantom, farther from the selected subset of antenna positions when compared to ALN-1 position.

The average response in all three tests is very similar, with SMR ranging from 8.69 to 8.95 dB. The FWHM metric shows that the overall spatial resolution of the ALN response is low, which is common in MWI systems and particularly in this application is affected by the limited angular range imposed by the torso. Nonetheless, the ALN responses are detected in the correct position.

We believe these preliminary results demonstrate the potential of MWI to assess ALNs detection, although further assessment must be performed before considering clinical tests.

V. Conclusion

We presented a detailed methodology and promising results from the first tests to detect ALNs using MWI technology. MWI may be a useful complementary diagnostic tool for metastasised level I ALNs and potentially decrease the false negative and false positive rates of ALNs diagnosis ahead of surgery.

The results show the robustness of the method to the complex and non-uniform body region of the axilla. The performance metrics show a SCR higher than 1.5 dB and a LE lower than the ALNs dimensions in the performed tests.

The work presented in this paper is a significant technological and methodological contribution in the area of MWI towards the detection of level I ALNs in an experimental scenario. We developed and presented a full pre-clinical system comprising the mechanical setup, axillary realistic phantoms and algorithms designed for ALN imaging, addressing the challenges that imaging the axillary region presents, which are mainly related to its morphology and anatomy. We showed that a cylindrical antenna sweep a few centimetres away from the phantom surface in air and in an experimental volumetric setup, with similar conditions to a clinical scenario, provides promising results in detecting level I ALNs. The proposed configuration is also suitable for axillary imaging since it does not limit the number of antenna positions surrounding a limited volume such as the axillary region. Furthermore, we established solutions for the limitations inherent to the morphology of the region of interest that are significantly different from other well-studied applications (i.e. breast or brain). For this purpose, we removed artefacts considering neighbour antenna positions decreasing the variability of the distance from the antenna to the phantom surface and performed an automatable search to find an optimal group of antenna positions for imaging the axillary region. We also applied a spatial filter to select the volume of interest, which is of utmost importance in such non-uniform anatomical shape such as the axillary region with ALNs surrounded by other anatomical structures of the torso. Information on patient-specific biometrics for this volume is also important to ensure ALNs detection.

In future work, further tests will be performed to validate this system, such as considering other axillary region models, imaging multiple level I ALNs and differentiating healthy and metastasised ALNs. We intend to increase the phantom complexity, by adding muscle mimicking materials, and also by adding a dielectric-representative skin layer. It is also important to adequately model the complex permittivity of both healthy and metastasised ALNs. Hence, the dielectric properties of ALNs should also be updated according to new data, once it becomes available. Finally, the Specific Absorption Rate (SAR) of our system will also be assessed in a future stage, although we are using the same power level as for breast MWI in which we found safe SAR values.

Acknowledgment

The authors would like to thank António Almeida for his help with the setup creation and measurements, Dr. Maria de Lurdes Orvalho at Hospital da Luz Lisboa for her clinical

expertise, Dr. Durval Costa at Champalimaud Foundation for providing the CT image used to create the axillary phantom under protocol "MMWave" (17/10/2018), and Duarte Guerreiro for initial processing of the images so the axillary region model could be printed in 3D.

REFERENCES

[1] World Health Organization, "Breast Cancer Fact Sheets," 2020. [Online]. Available: http://gco.iarc.fr/today

[2] American Joint Committee on Cancer, "Breast Cancer," in *AJCC Cancer Staging Manual*, 8th ed. Springer, 2018.

[3] S. M. Dudea, M. Lenghel, C. Botar-Jid, D. Vasilescu, and M. Duma, "Ultrasonography of superficial lymph nodes: Benign vs. malignant," *Med. Ultrason.*, vol. 14, no. 4, pp. 294–306, 2012.

[4] V. E. Mortellaro *et al.*, "Magnetic Resonance Imaging for Axillary Staging in Patients With Breast Cancer," *J. Magn. Reson. Imaging*, vol. 30, pp. 309–312, 2009.

[5] P. A. Baltzer *et al.*, "Application of MR mammography beyond local staging: Is there a potential to accurately assess axillary lymph nodes? Evaluation of an extended protocol in an initial prospective study," *AJR. Am. J. Roentgenol.*, vol. 196, no. 5, pp. 641–647, 2011.

[6] G. R. Kim *et al.*, "Preoperative axillary US in early-stage breast cancer: Potential to prevent unnecessary axillary lymph node dissection," *Radiology*, vol. 288, no. 1, pp. 55–63, 2018.

[7] G. Viale *et al.*, "Predicting the status of axillary sentinel lymph nodes in 4351 patients with invasive breast carcinoma treated in a single institution," *Cancer*, vol. 103, no. 3, pp. 492–500, 2005.

[8] G. H. Sakorafas, G. Peros, L. Cataliotti, and G. Vlastos, "Lymphedema following axillary lymph node dissection for breast cancer," *Surg. Oncol.*, vol. 15, pp. 153–165, 2006.

[9] A. Lucci *et al.*, "Surgical Complications Associated With Sentinel Lymph Node Dissection (SLND) Plus Axillary Lymph Node Dissection Compared With SLND Alone in the American College ofSurgeons Oncology Group Trial Z0011," *Int. J. Clin. Oncol.*, vol. 25, no. 24, pp. 3657–3663, 2007.

[10] E. C. Fear, J. Bourqui, C. Curtis, D. Mew, B. Docktor, and C. Romano, "Microwave breast imaging with a monostatic radar-based system: A study of application to patients," *IEEE Trans. Microw. Theory Techn.*, vol. 61, no. 5, pp. 2119–2128, 2013.

[11] A. W. Preece, I. Craddock, M. Shere, L. Jones, and H. L. Winton, "MARIA M4: clinical evaluation of a prototype ultrawideband radar scanner for breast cancer detection," *J. Med. Imaging*, vol. 3, no. 3, pp. 1–7, 2016.

[12] M. Shere, I. Lyburn, R. Sidebottom, H. Massey, C. Gillett, and L. Jones, "MARIA® M5: A multicentre clinical study to evaluate the ability of the Micrima radio-wave radar breast imaging system (MARIA®) to detect lesions in the symptomatic breast," *Eur. J. Radiol.*, vol. 116, pp. 61–67, 2019.

[13] J. A. Vasquez *et al.*, "A Prototype Microwave System for 3D Brain Stroke Imaging," *Sensors*, vol. 20, no. 9, pp. 1–16, 2020.

[14] O. Karadima *et al.*, "Experimental Validation of Microwave Tomography with the DBIM-TwIST Algorithm for Brain Stroke Detection and Classification," *Sensors*, vol. 20, no. 3, pp. 840–856, 2020.

[15] U. Veronesi *et al.*, "Distribution of axillary node metastases by level of invasion. An analysis of 539 cases," *Cancer*, vol. 59, no. 4, pp. 682–687, 1987.

[16] P. P. Rosen, M. L. Lesser, D. W. Kinne, and E. J. Beattie, "Discontinuous or 'skip' metastases in breast carcinoma. Analysis of 1228 axillary dissections," *Annals of Surgery*, vol. 197, no. 3, pp. 276–283, 1983.

[17] G. C. Bentel, L. B. Marks, P. H. Hardenbergh, and L. R. Prosnitz, "Variability of the depth of supraclavicular and axillary lymph nodes in patients with breast cancer: Is a posterior axillary boost field necessary?" *Int. J. Radiat. Oncol. Biol. Phys.*, vol. 47, no. 3, pp. 755–758, 2000.

[18] B. Ludescher, M. Rommel, T. Willmer, A. Fritsche, F. Schick, and J. MacHann, "Subcutaneous adipose tissue thickness in adults - Correlation with BMI and recommendations for pen needle lengths for subcutaneous self-injection," *Clin. Endocrinol.*, vol. 75, no. 6, pp. 786–790, 2011.

[19] M. Houshyari, A. S. Y. Kashi, S. S. Varaki, A. Rakhsha, and E. R. Blookat, "Regional lymph node radiotherapy in breast cancer: single anterior supraclavicular field vs. two anterior and posterior opposed supraclavicular fields." *Electron. Physician*, vol. 7, no. 2, pp. 1032–1038, 2015.

[20] S. Standring, "Blood, lymphoid tissues and haemopoiesis," in *Gray's Anatomy: The Anatomical Basis of Clinical Practice*, 41st ed. Elsevier Limited, 2016, pp. 68–80.

[21] M. B. Mainiero, C. M. Cinelli, S. L. Koelliker, T. A. Graves, and M. A. Chung, "Axillary Ultrasound and Fine-Needle Aspiration in the Preoperative Evaluation of the Breast Cancer Patient: An Algorithm Based on Tumor Size and Lymph Node Appearance," *AJR. Am. J. Roentgenol.*, vol. 195, no. 5, pp. 1261–1267, 2010.

[22] H. Rahbar *et al.*, "Suspicious Axillary Lymph Nodes Identified on Clinical Breast MRI in Patients Newly Diagnosed with Breast Cancer: Can Quantitative Features Improve Discrimination of Malignant from Benign?" *Acad. Radiol.*, vol. 22, no. 4, pp. 430–438, 2015.

[23] W. T. Joines, Y. Zhang, C. Li, and R. L. Jirtle, "The measured electrical properties of normal and malignant human tissues from 50 to 900 MHz," *Med. Phys.*, vol. 21, no. 4, pp. 547–550, 1994.

[24] J. W. Choi *et al.*, "Microwave detection of metastasized breast cancer cells in the lymph node; potential application for sentinel lymphadenectomy," *Breast Cancer Res. Treat.*, vol. 86, no. 2, pp. 107–115, 2004.

[25] T. R. Cameron, M. Okoniewski, and E. C. Fear, "A Preliminary Study of the Electrical Properties of Healthy and Diseased Lymph Nodes," in *Proc. 14th Int. Symp. Antenna Technol. Appl. Electromagn. and Am. Electromagn. Conf. (ANTEM/AMEREM)*, Ottawa, ON, Canada, 2010, pp. 1–3.

[26] R. J. N. Eleutério, "Microwave Imaging of the Axilla to Aid Breast Cancer Diagnosis," Master's Dissertation, Faculdade de Ciências e Tecnologia, Universidade Nova de Lisboa, 2014.

[27] J. M. Felício, J. M. Bioucas-Dias, J. R. Costa, and C. A. Fernandes, "Microwave Breast Imaging using a Dry Setup," *IEEE Trans. Comput. Imag.*, vol. 6, pp. 167–180, 2020.

[28] A. Vispa *et al.*, "UWB device for breast microwave imaging: phantom and clinical validations," *Measurement*, vol. 146, pp. 582–589, 2019.

[29] M. T. Islam, M. Z. Mahmud, M. T. Islam, S. Kibria, and M. Samsuzzaman, "A Low Cost and Portable Microwave Imaging System for Breast Tumor Detection Using UWB Directional Antenna array," *Sci. Rep.*, vol. 9, no. 1, pp. 1–13, 2019.

[30] T. Reimer, M. Solis-Nepote, and S. Pistorius, "The Application of an Iterative Structure to the Delay-and-Sum and the Delay-Multiply-and-Sum Beamformers in Breast Microwave Imaging," *Diagnostics*, vol. 10, no. 6, pp. 411–426, 2020.

[31] J. M. Felício, C. A. Fernandes, and J. R. Costa, "Complex Permittivity and Anisotropy Measurement of 3D-Printed PLA at Microwaves and Millimeter-waves," in *Proc. 22nd Int. Conf. Appl. Electromagnetics Commun. (ICECOM)*, Dubrovnik, Croatia, 2017, pp. 1–6.

[32] N. Joachimowicz, B. Duchêne, C. Conessa, and O. Meyer, "Anthropomorphic Breast and Head Phantoms for Microwave Imaging," *Diagnostics*, vol. 8, no. 4, pp. 85–97, 2018.

[33] Embodi3D, "Kidney 3D STL," 2019. [Online]. Available: https://www.embodi3d.com/files/file/23187-kidney-3d-stl-file/

[34] D. M. Godinho *et al.*, "Extracting Dielectric Properties for MRI-based Phantoms for Axillary Microwave Imaging Device," in *14th European Conference on Antennas and Propagation, EuCAP 2020*, Copenhagen, Denmark, 2020, pp. 3–6.

[35] N. Joachimowicz, C. Conessa, T. Henriksson, and B. Duchêne, "Breast Phantoms for Microwave Imaging," *IEEE Antennas Wireless Propag. Lett.*, vol. 13, pp. 1333–1336, 2014.

[36] S. Gabriel, R. W. Lau, and C. Gabriel, "The dielectric properties of biological tissues: III Parametric models for the dielectric spectrum of tissues," *Physics in Medicine and Biology*, vol. 41, no. 11, pp. 2271–2293, 1996.

[37] M. Lazebnik *et al.*, "A large-scale study of the ultrawideband microwave dielectric properties of normal breast tissue obtained from reduction surgeries," *Physics in Medicine and Biology*, vol. 52, no. 10, pp. 2637–3656, 2007.

[38] J. M. Felício, J. M. Bioucas-Dias, J. R. Costa, and C. A. Fernandes, "Antenna Design and Near-Field Characterization for Medical Microwave Imaging Applications," *IEEE Trans. Antennas Propag.*, vol. 67, no. 7, pp. 4811–4824, 2019.

[39] D. Kurrant, J. Bourqui, and E. Fear, "Surface Estimation for Microwave Imaging," *Sensors*, vol. 17, no. 7, pp. 1658–1678, 2017.

[40] D. M. Godinho, J. M. Felício, C. A. Fernandes, and R. C. Conceição, "Evaluation of Refraction Effects in Dry Medical Microwave Imaging Setups," *IEEE Antennas Wireless Propag. Lett.*, vol. 20, no. 4, pp. 617–621, 2021.

[41] D. O'Loughlin, "Improving the Sensitivity of Radar-based Breast Imaging Algorithms in Diverse Patient Populations," Ph.D. dissertation, National University of Ireland Galway, 2018.

Daniela M. Godinho was born in Fundão, Portugal, in 1994. She received an Integrated Master degree in Biomedical Engineering from Universidade Nova de Lisboa, Portugal, in October 2016. She is currently a Ph.D. student in Faculdade de Ciências, Universidade de Lisboa, Portugal, and has been working on Microwave Imaging to aid breast cancer diagnosis and staging. Her research interests rely on areas such as medical imaging, signal and image processing, and machine learning.

João M. Felício was born in Lisbon, Portugal, in 1990. He received the MSc and PhD degrees in Electrical and Computer Engineering from the Instituto Superior Técnico (IST), University of Lisbon, Lisbon, in 2014 and 2018, respectively. He is a Professor at Escola Naval, Alfeite, Portugal, and a researcher at Centro de Investigação Naval (CINAV) and Instituto de Telecomunicações. His main interests include microwave imaging, antenna design, and antennas for biomedical applications.

Carlos A. Fernandes (S'86-M'89-SM'08) received the Licenciado, MSc, and Ph.D. degrees in Electrical and Computer Engineering from Instituto Superior Técnico (IST), Technical University of Lisbon, Lisbon, Portugal, in 1980, 1985, and 1990, respectively. He joined IST in 1980, where he is presently Full Professor at the Department of Electrical and Computer Engineering in the areas of microwaves, radio wave propagation and antennas. He is a senior researcher at the Instituto de Telecomunicacões and member of the Board of Directors. He has co-authored a book, 2 book chapters, more than 200 technical papers in peer reviewed international journals and conference proceedings and 7 patents in the areas of antennas and radiowave propagation modeling. His current research interests include dielectric antennas for millimeter wave applications, antennas and propagation modeling for personal communication systems, RFID and UWB antennas, artificial dielectrics and metamaterials. He was a Guest Editor of the Special Issue on "Antennas and Propagation at mm- and Sub mm-Waves", from the IEEE Transactions on Antennas and Propagation, April 2013.

Raquel C. Conceição was born in Lisbon, Portugal in 1984. She holds a Ph.D. in Electrical and Electronic Engineering (2011) from the National University of Ireland Galway, and an Integrated Masters in Biomedical Engineering (2007) from the Faculdade de Ciências e Tecnologia, Universidade Nova de Lisboa, Portugal. She is an Assistant Professor at Faculdade de Ciências, Universidade de Lisboa, Portugal since 2016, and she is a full researcher at the Instituto de Biofísica e Engenharia Biomédica since 2012. She is the editor of two books: "An Introduction to Microwave Imaging for Breast Cancer Detection" (Springer 2016), and "Emerging Electromagnetic Technologies for Brain Diseases Diagnostics and Monitoring" (Springer 2018), and has published 68 peer-reviewed international journals and conference proceedings. Her main research interests comprise developing microwave imaging techniques to detect and classify breast cancer as well as axillary lymph nodes. Conceição is an URSI Individual Member (appointment for life) since 2017 and is a member of the Marie Curie Alumni Association (MCAA) since 2013.